Flight Performance of a multirotor unmanned aerial vehicle with digital displacement hydrostatic transmission

FLIGHT PERFORMANCE OF A MULTIROTOR UNMANNED AERIAL VEHICLE WITH DIGITAL DISPLACEMENT HYDROSTATIC TRANSMISSION

Calum Arnott[1,2], Rory Haggart[1], Robert Courtney[1,2], Uwe Stein[1], Francisca Martinez-Hergueta[2]

[1]Flowcopter Ltd, Edinburgh (UK)
[2]Institute for Infrastructure & Environment, School of Engineering, University of Edinburgh, Edinburgh (UK)

Abstract

This paper summarises the development of a hybrid multirotor UAV which uses a Digital Displacement® hydrostatic transmission. The design of Flowcopter's FC-100 demonstrator UAV is presented, along with a summary of the concept and the modelling equations of the propulsion system. Focus is placed on gaining a critical physical understanding of the rotor aerodynamic performance through experimental characterisation. To isolate the influence of interactional aerodynamic effects between rotors and with the airframe, the experimental campaign comprises testing at different levels; a single fixed-pitch rotor in static and translational flight conditions, and flight testing of the full-scale demonstrator UAV. The analysis of the aerodynamic ground effect demonstrates a greater effect than an equivalent helicopter. Test data shows a negligible effect on lift efficiency when hovering at wind speeds up to 11.2 m/s. Translational flight tests at airspeeds of up to 18.2 m/s demonstrate an increase in lift efficiency at lower speeds. An outlook towards future testing and development is presented.

1. INTRODUCTION

In recent years, there has been rapid growth in the development of electrical vertical take-off and landing (eVTOL) aircraft concepts, notably the Vertical Flight Society's eVTOL concept tracker reached 1000 unique designs in 2024 [1]. The proliferation of design concepts is due in part to the growing use of distributed electric propulsion systems to provide lift. Distributed propulsion systems may enable new aircraft architectures offering improved fuel efficiency and safety [2], [3].

Digital Displacement® (DD) hydraulic technology has emerged as an alternative to electric drive systems for distributed propulsion, offering a higher power density than an equivalent electric transmission [4]. This enables increased flight range and useful payload capacity for multirotor Unmanned Aerial Vehicles (UAVs) [5]. Compared to conventional hydraulics, DD technology boasts a higher efficiency, faster control response, and elimination of hysteresis [6], [7], [8].

Flowcopter Ltd, based in Edinburgh (UK), has developed a heavy-lift utility UAV which utilises a DD hydrostatic transmission. Previous work [4] introduced the concept of the DD hydrostatic transmission for distributed propulsion in rotorcraft, alongside the design of Flowcopter's initial 'H-380' proof-of-concept drone. Subsequent work [5] progressed the H-380 concept, presenting rotor performance data from ground-based testing of the system. Since 2021, Flowcopter has focused development on its 'FC-100' pre-production UAV demonstrator, a 500 kg platform at maximum take-off weight.

A key challenge in the design and performance evaluation of large multirotor UAVs is the accurate characterisation of their power requirement during all flight stages. Helicopters typically benefit from a significant reduction in the power required for forward flight [9], [10]. Some research suggests that, compared to an equivalent sized helicopter, quadrotor UAVs may have an increased power requirement in forward flight, due to unfavourable aerodynamic interactions between the front and rear rotors on the UAV [11],

[12]. However, validation of this result with experimental data has not been possible, as research to date has focused predominantly on the performance of small-scale quadrotor UAVs with a take-off weight less than 5 kg [13], [14], [15], [16], [17]. These findings cannot be directly translated to develop larger platforms with fixed-pitch rotors operating at a much higher Reynold's number and a higher disc loading. Therefore, additional efforts are needed to study the aerodynamic performance of large-scale multirotor UAVs through experimental testing. This will provide validation data for flight models that can be used to design and optimise large-scale UAVs in the future.

This paper presents the design of Flowcopter's FC-100 UAV and investigates its aerodynamic performance through experimental testing of the rotors in static and dynamic conditions, and full-system testing both indoors and in windy environmental conditions outdoors. A static thrust test rig and a dynamic towed test rig are used to simulate forward flight conditions of over 100 km/h. Subsequently, indoor and outdoor flight testing of the FC-100 platform in both environments enables the analysis of the aerodynamic ground-effect and the power performance in windy environmental conditions during both hover and forward flight tests.

2. SUMMARY OF FC-100 DESIGN

Flowcopter's FC-100 multirotor UAV, designed with a 500 kg maximum take-off weight, is shown in Figure 1. It has been developed principally as a utility platform targeting applications in humanitarian aid delivery, offshore logistics, search and rescue, agriculture and other applications in harsh environments which require a combination of sustained hover capability, long flight endurance and high payload capacity.

Figure 1: FC-100 UAV

A summary of the basic parameters of the FC-100 are described in Table 1.

Table 1: FC-100 basic design parameters

Parameter [units]	Value
Frame dimensions[a] [m]	2.56 x 2.45 x 2.01
Empty weight [kg]	350
Payload + fuel weight [kg]	150
Max. take-off weight (MTOW) [kg]	500
Engine power peak/continuous [kW]	104/99
Approx. fuel burn rate in hover [kg/h]	25
Number of rotors [-]	4
Blades per rotor [-]	3
Rotor diameter [m]	2.35
Hover disc loading at MTOW [kg/m^2]	~26

[a] *(Length x Width x Height)*

The prime mover of the FC-100 is a Rotax-915is liquid fuel combustion engine, providing up to 99 kW of continuous power. This is coupled to a Digital Displacement® Pump (DDP), a radial piston pump which has four independently controllable hydraulic outputs, the theory and operation of which has been detailed extensively [6], [7], [8]. Each of the pump's independent outlets provides flow of hydraulic oil to a bent-axis fixed displacement hydraulic motor. These motors are used to drive the rotors which produce lift. A hydraulic diagram of the transmission is shown in Figure 2.

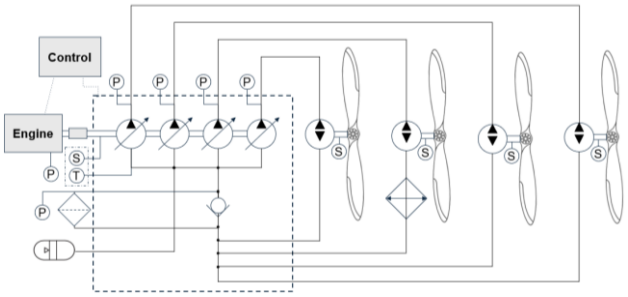

Figure 2: Hydraulic schematic of power transmission

The operation of the control system and the hardware used is detailed in Figure 3. To control the attitude (pitch, roll and yaw angles) and altitude of the UAV, a Cubepilot Orange commercial off-the-shelf flight controller is used. The flight controller sends thrust commands which are interpreted by a system controller which has two main functions:

1. Control of the rotational speed of the rotors – achieved by a feedback control loop which

involves converting the thrust commands from the flight controller into flow commands for the DDP and measuring the rotational speeds of the rotors by on-board tachometers.

2. Control of the engine speed – achieved by a combination of feedback and feedforward control loops on the angle of the throttle valve on the engine, which is adjusted to maintain constant engine speed under varying load.

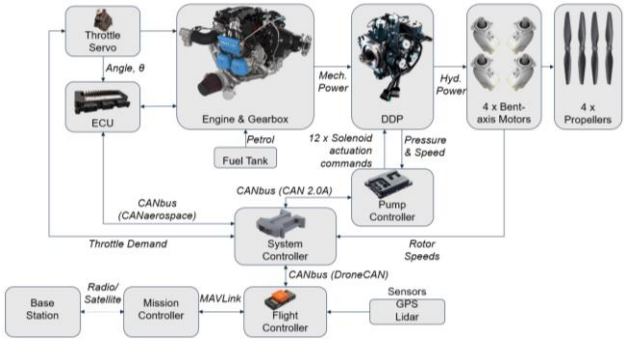

Figure 3: Control System Architecture

3. MODELLING EQUATIONS OF THE PROPULSION SYSTEM

To provide context for later analysis, the equations presented here describe a 1D model of the digital hydraulic propulsion system. This consists of the engine, gearbox, pump, motors and rotors.

The displacement of a hydraulic pump is the amount of fluid per revolution which is pumped into the delivery port. The displacement D_p of the Digital Displacement pump reduces from the geometric displacement $D_{p,geom}$ with pressure primarily due to the effect of fluid compressibility at high rotational speed, captured by constant k_p [7], and is varied by the time-averaged fraction F_d of the cylinders which are enaled in a sequence generated by the Pump Controller:

$$D_p = \left(D_{p,geom} - p \cdot k_p\right) \cdot F_d \tag{1}$$

The flow displaced by the pump Q_p enters the high-pressure section of the hydraulic circuit:

$$Q_p = D_p \cdot \omega_p \tag{2}$$

Where ω_p is the pump rotational speed.

Each independently controlled motor is provided with a group of pump cylinders with a separate high-pressure output, called a “pumplet.” The flow absorbed by the motor Q_m is higher than expected from the geometric displacement, D_m, due to leakage and compressibility effects, which are included within the volumetric efficiency term $\eta_{vol,m}$:

$$Q_m = D_m \cdot \omega_m \, \eta_{vol,m} \tag{3}$$

Where ω_m is the motor rotational speed.

The difference between pump flow in, and motor flow out of the circuit, accumulates in the fluid compliance flow of the high-pressure section of the circuit, Q_c. This compliance is not a discrete component but a model of the effect of bulk modulus and hose volumetric elastic expansion:

$$Q_c = Q_p - Q_m \tag{4}$$

The pressure is proportional to the volume accumulated in the compliance:

$$p = k_c \cdot \int Q_c \tag{5}$$

Where k_c is a constant.

The torque generated by the motor τ_m is proportional to the mechanical efficiency, $\eta_{mech,m}$:

$$\tau_m = D_m \cdot p \cdot \eta_{mech,m} \tag{6}$$

The energy losses in the pump are represented by the overall efficiency, which increases the torque exerted by the pump:

$$\tau_p = \frac{D_p \cdot p}{\eta_{total,p}} \tag{7}$$

The aerodynamic torque, τ_r, and thrust, T, of the rotor are proportional to the square of the rotor angular velocity ω_r , and vary as a function of the advance ratio, $\mu = v \cos\theta / R\omega_r$, and inflow ratio, $\lambda = (v_i + v \sin\theta) / R\omega_r$:

$$\tau_r = k_\tau \cdot \omega_r^2 \cdot K_\tau(\mu, \lambda) \tag{8}$$

$$T = k_T \cdot \omega_r^2 \cdot K_T(\mu, \lambda) \tag{9}$$

The total torque exerted by the pump on the gearbox output shaft is the sum of the torque of the pumplets:

$$\tau_{p,total} = \sum_{1}^{n} \tau_p[n] \tag{10}$$

The gearbox links the torque and speed according to the gear ratio, k_g:

$$\tau_g = \frac{\tau_{p,total}}{k_g} \quad (11)$$

$$\omega_p = \omega_e \cdot k_g \quad (12)$$

The engine generates torque as a function of its speed, the throttle angle set by the controller, and time constant effects:

$$\tau_e = f(\omega_e, \theta, t) \quad (13)$$

The engine is modelled as an inertia acted on by the engine torque, and the gearbox load:

$$\omega_e = \frac{1}{I_e}\int(\tau_e - \tau_g) \quad (14)$$

The rotor is modelled as an inertia acted on by the motor torque, and the rotor aerodynamic load:

$$\omega_r = \frac{1}{I_r}\int(\tau_m - \tau_r) \quad (15)$$

For rotor analysis, the ideal induced velocity is calculated from thrust T, air density ρ and rotor area A:

$$v_i = \sqrt{\frac{T}{2\rho A}} \quad (16)$$

The ideal rotor power is:

$$P_{ideal} = v_i \cdot T \quad (17)$$

Using Eq. 8, the actual rotor power is:

$$P_{actual} = \tau_r \cdot \omega_r = k_\tau \cdot \omega_r^3 \cdot K_\tau(\mu, \lambda) \quad (18)$$

The rotor's Figure of Merit, FM, can then be calculated by:

$$FM = \frac{P_{ideal}}{P_{actual}} \quad (19)$$

Combining Eq. 16, 17 & 19, the actual rotor power can be written as:

$$P_{actual} = (FM)^{-1} \cdot T \cdot \sqrt{\frac{T}{2\rho A}} \quad (20)$$

Where *T/A* is the rotor disc loading, which defines the thrust per rotor disc swept area.

The thrust to power ratio of the rotor, henceforth denoted the 'lift efficiency' LE, is calculated by:

$$LE = \frac{T}{P_{actual}} \quad (21)$$

Where the 'effective lift efficiency', LE_e, at the engine accounts for the transmission efficiency:

$$LE_e = \frac{T}{P_{actual}}\eta_{trans} = \frac{T}{P_{engine}} \quad (22)$$

The transmission efficiency lumps the total pump efficiency and motor mechanical efficiency terms:

$$\eta_{trans} = \eta_{total,p} \cdot \eta_{mech,m} \quad (23)$$

By combining Eq. 20 & 21, the lift efficiency is related to the rotor disc loading and Figure of Merit by:

$$LE = \frac{T}{P_{actual}} = \sqrt{2\rho} \cdot FM \cdot \left(\frac{T}{A}\right)^{-\frac{1}{2}} \quad (24)$$

4. STATIC ROTOR TESTING

4.1. Test Rig

A transmission test rig was developed to evaluate the performance of a single rotor in static conditions. The test rig comprises a propulsion unit consisting of a rotor mounted to a bent-axis hydraulic motor which is driven by a DDP096 Digital Displacement® pump (see Figure 4). The prime mover of the DDP is a 30kW 3-phase electric motor, the rotational speed of which is controlled by a variable frequency inverter. The data acquisition unit utilised is a Dewesoft DEWE-43a with 24-bit ADCs, digital inputs with 100 MHz counter, and synchronised CAN message acquisition.

As described by Eq. 2, the flow output from the DDP is set by commanding the desired flow displacement at a given crankshaft rotational speed. Commands are sent via a desktop PC to the integrated DDP controller (DPC-12) which controls the flow rate of the DDP outlets by selectively closing or leaving open the low-pressure valves in each cylinder once per cycle.

In the case of the static rotor test rig, only one of the four outlet services from the DDP is used to supply flow to the hydraulic motor. By varying the rotational speed of the electric motor and flow displacement command of the DDP, the flow rate to the bent-axis hydraulic motor is varied, thus controlling the rotor rotational speed.

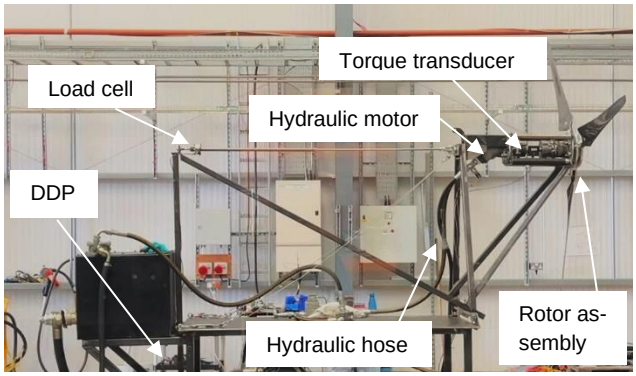

Figure 4: Static rotor test rig

A load cell is mounted in line with the rotor to measure the thrust force that it produces at a set rotational speed. An integrated torque and tachometric speed transducer is installed between the hydraulic motor and rotor assembly to measure the mechanical power delivered to the rotor. The hardware used on the test rig is detailed in Table 2.

Table 2: Test rig hardware

Component	Details
Bent-axis hydraulic motor	Sunfab SAP034 optimised, 34 cc/rev
Load cell	0-500 kg tension/compression
Torque & tachometric speed transducer	DRFL 200 Nm
Flowmeter	Webtec LT60-FM-B-B-6
Pressure transducers	LP: Danfoss 4-20 mA, -1-9 bar HP: Danfoss 4-20 mA, 0-600 bar
Rotor speed sensor	Honeywell SNDH-H3C-G04
DDP controller	Danfoss DPC-12
Data acquisition	Dewesoft DEWE-43a

4.2. Results

A rotor test is conducted at different rotational speeds to measure the thrust and power performance curves. The speed ramp is controlled manually via the desktop PC.

As shown in Figure 5 & Figure 6, the thrust increases with the square of the rotational speed, and the mechanical power requirement with the cube of the rotational speed, aligning well with the theory described in Eq. 9 & 18, respectively.

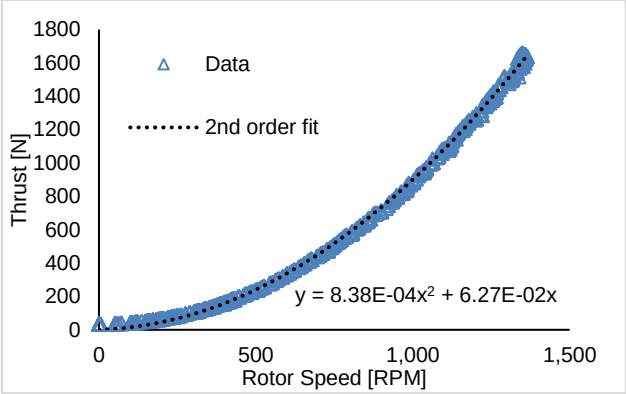

Figure 5: Thrust vs rotor speed

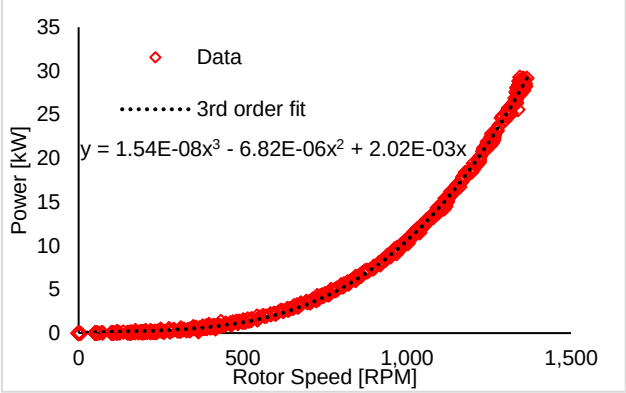

Figure 6: Power vs rotor speed

To evaluate the aerodynamic performance of the rotor, the Figure of Merit (FM) is calculated at different rotor speeds according to Eq. 19, shown in Figure 7. There is a wide variance in the data values at speeds below 800 rpm, which is likely due to observed resonant vibrations of the test rig at lower blade passing frequencies. It may also be a blade inertial effect due to increased pressure pulsation at the motor at low rotational speeds due to the method of operation used on the test rig.

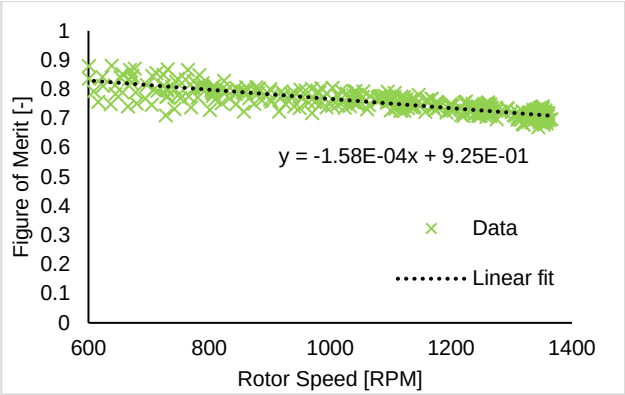

Figure 7: Figure of Merit vs rotor speed

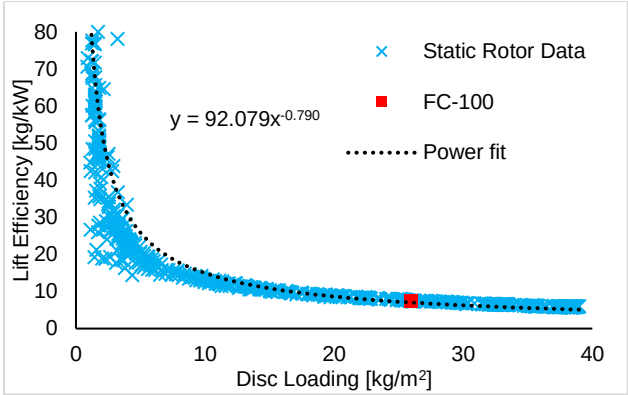

Figure 8: Lift efficiency vs disc loading

The trendline shows that the FOM decreases linearly with increased rotor speed. This is likely due to the increased blade loading at higher rotational speeds resulting in changes to effective blade geometry due to greater flap-wise bending and torsional deflection with increasing load. Future blade testing should aim to quantify this deflection to maximise efficiency across the operational speed range.

The relationship between lift efficiency of the rotor and disc loading is shown in Figure 8. A power curve is fitted to the data, as per the relationship in Eq. 24. It should be noted that Eq. 24 does not capture the more complex physics of the rotor, such as the FM varying with rotational speed (Figure 7). However, it looks to underestimate the lift efficiency at the disc loading value corresponding to the maximum take-off weight (MTOW) of the UAV. Thus, it provides a worst-case initial estimate of the rotor power requirement.

The lift efficiency (Eq. 21) of the rotor is considered at the vehicle disc loading design point. The disc loading of the rotor in hover at vehicle MTOW (see Table 1) is approximately 26 kg/m^2, and at this point, the calculated lift efficiency from the fitted curve is 7.02 kg/kW (see Figure 8). To establish the effective lift efficiency at the engine, the transmission efficiency is first calculated to be 86% with Eq. 23, assuming a DDP efficiency of 94% based on previous test results [4] and motor efficiency of 92% (manufacturer data in Appendix A). The effective lift efficiency is calculated to be 6.04 kg/kW using Eq. 22.

5. TOWED ROTOR TESTING

5.1. Test Rig

A test rig was developed to evaluate the aerodynamic performance of a single rotor in forward flight conditions for different tilt angles of the rotor (see Figure 9). This is to emulate the non-zero pitch angle of the UAV required to fly forward.

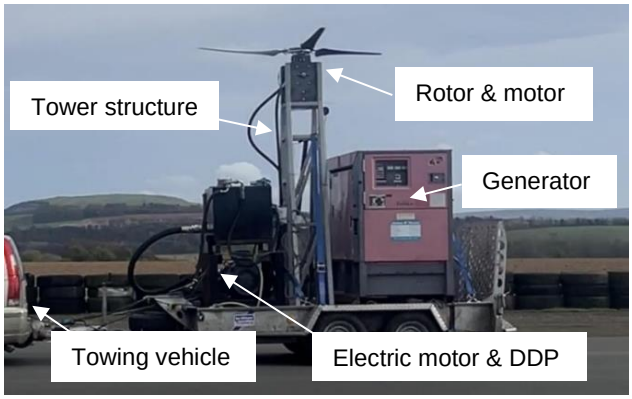

Figure 9: Towed rotor test rig at East Fortune racetrack, Scotland (March 2024)

The test rig consists of a rotor attached to a hydraulic motor mounted atop a welded structure. The mount is constrained axially by a load cell which is used to measure thrust production. The mount is on linear rails, allowing small axial deflection before hard stopping against the load cell (see Figure 10). The structure is installed on a trailer, with a generator used to supply power to the 30 kW electric motor which is used to drive the DDP – as used in the static test rig. The trailer can then be towed by a vehicle, to emulate the forward flight conditions of the rotor on the UAV.

The instrumentation and hardware used on the test rig is the same as detailed in Table 2, however a torque transducer was not used due to packaging issues. To measure the airspeed of the trailer, a pitot

tube was mounted to the side of the towing vehicle. However, a fault with the instrument during testing meant that a back-up anemometer was used as the principal airspeed measurement instrument, thus limiting the measurement precision.

By considering only the steady-state behaviour of the rotor, calculation of the power required is made using Eq. 18, in which the load torque of the rotor is balanced by the torque produced by the motor, described by Eq. 15. The mechanical efficiency of the pump is assumed to be 92% based on the manufacturer's test data (see Appendix 1).

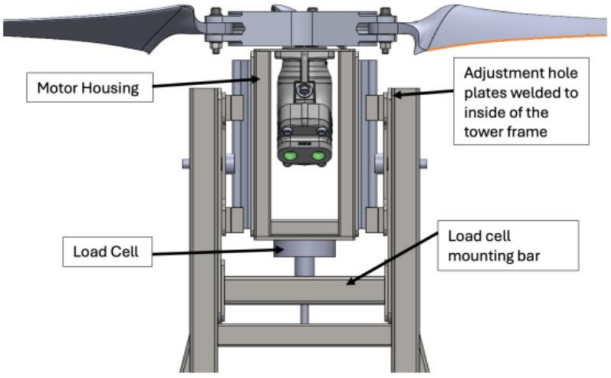

(a)

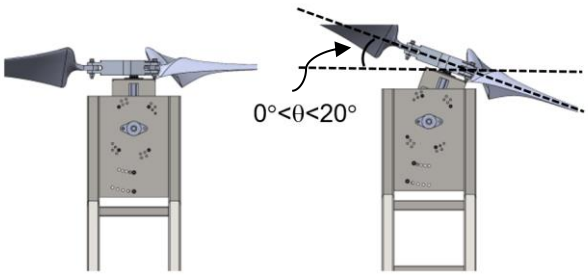

(b)

Figure 10: Test frame adjustability of the pitch angle of the rotor and motor mounting, (a) front view (b) side view.

5.2. Results

Three tests were conducted at East Fortune motorbike track, near Edinburgh. Three rotor tilt angles of 0, 5, and 10 degrees were tested. For each test case, the flow rate to the motor was set such that the rotor ran at a fixed speed of 1050 rpm, producing 100 kg of thrust in static flow conditions (see Figure 5).

During the tests, the towing vehicle was steadily accelerated along the track to a speed of approximately 110 km/h before a steady deceleration to a stop. The resultant thrust produced by the rotor was measured for the duration of the test, with the data presented for each rotor tilt angle in Figure 11 and Figure 12. It can be noted that there is a large variance in the data at each velocity, which is likely due to limitations in measurement precision using the anemometer and variance in wind conditions.

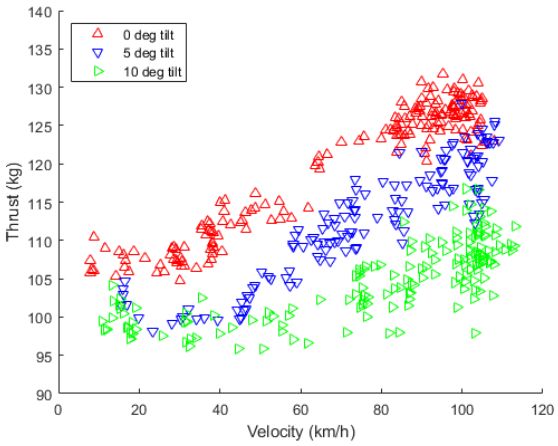

Figure 11: Thrust vs forward velocity as a function of rotor disc tilt angle

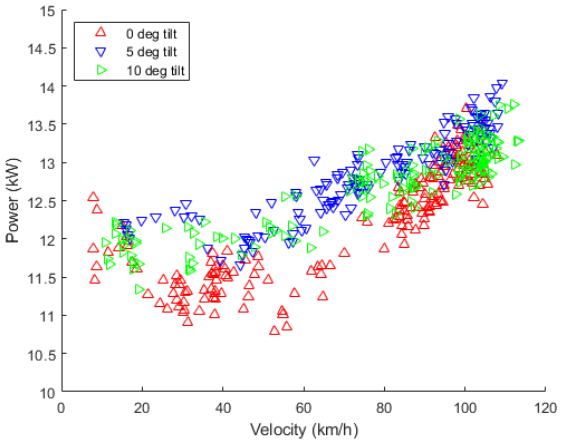

Figure 12: Power vs forward velocity as a function of rotor disc tilt angle

It is observed that for each tested tilt angle of the rotor disc plane, the thrust increases with forward velocity. The greatest increase in thrust is measured in the pure-edgewise flight case (0° tilt) whereby the inflow ratio is minimised. The effect of forward velocity improving thrust generation is observed to decrease with increasing rotor disc tilt angle, corresponding to

a reduction in the advance ratio and an increase in the inflow ratio.

A comparison of the power data reveals that, for tilt angles of 0 and 5 degrees, there is a decrease in power with initial increase in forward flight speed, before the power increases again at higher flight speeds. The initial decrease in power requirement is attributed to a reduction in the induced component of power as the inflow angle reduces with respect to the rotor disc plane, resulting in a higher effective angle of attack [9]. The increase in power at higher flight velocities is attributed to the profile (viscous) loss of the rotor blade, which has a 3rd order proportionality to the flight velocity – thus being a dominant component of total rotor power loss at high velocities. For the 10-degree tilt, it is not clear if there is a decrease in power requirement initially before it increases at higher speed. Future testing should aim to improve measurement instrumentation to better quantify the power requirement at lower speeds of up to 40 km/h.

To compare the relative performance of the rotor at different rotor disc tilt angles, the lift efficiency is calculated and shown in Figure 13. The greatest improvement in lift-efficiency with increasing flight velocity is achieved in the purely edgewise case (0° tilt), with the improvement in lift efficiency reducing for increasing rotor disc tilt angle. For 10-degree tilt, it cannot be concluded from the data that there is improvement in the lift efficiency with increasing forward velocity above 40 km/h.

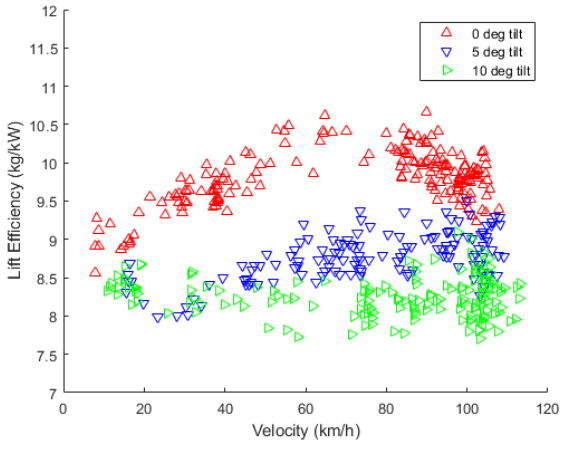

Figure 13: Lift efficiency vs forward velocity as a function of rotor tilt angle

The percentage improvement in lift efficiency between static conditions and medium flight speed (60 km/h) is compared in Table 3.

Table 3: Lift efficiency improvement for different rotor disc tilt angles at 60 km/h flight velocity.

Tilt angle	Average Lift Efficiency [kg/kW]		
	V = 0 km/h	V = 60 km/h	Δ%
0° tilt	7.7[a]	9.9	+29%
5° tilt	7.7[a]	9.0	+17%
10° tilt	7.7[a]	8.1	+5%

[a]*Lift efficiency calculated from static data (see Section 4)*

6. FULL-SCALE FC-100 UAV TESTING

6.1. Indoor testing

Following successful indoor ground-based testing, detailed in a previous paper [5], Flowcopter progressed to testing the FC-100 in November 2023 in an indoor environment, without tethers or a fall-arrest system, as shown in Figure 14.

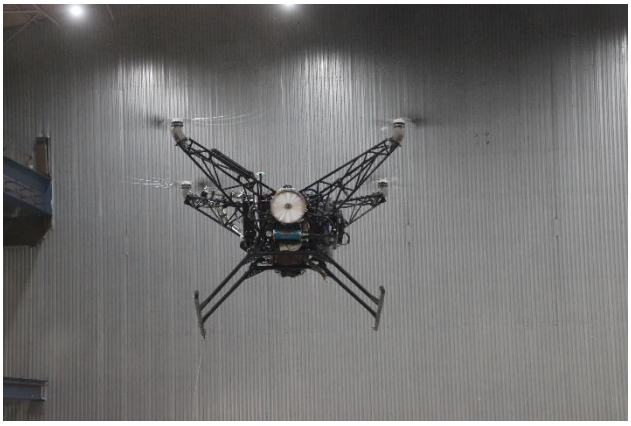

Figure 14: FC-100 indoor flight, November 2023. Flight video available [18]: https://youtu.be/SsixCnz-BZb0?si=u4mazUOsJVeAiv2r

During these indoor flight trials, the UAV was flown in a controlled hover at different heights above ground level to evaluate the effect of the aerodynamic ground effect, in which an increase in thrust production without increased power requirement is observed as the aircraft is closer to the ground, a well investigated phenomenon in helicopters [19], [20], [21] and small multirotor UAVs [22], [23], [24], [25].

Flight test data collected is evaluated against two established empirical models. Firstly, Hayden's [20] ground-effect model for helicopters was considered:

$$P_{IGE} = k_G^{-1} P_{OGE} \quad (25)$$

Where P_{IGE} is the power in ground effect and P_{OGE} is the power out of ground effect. The term k_G is described by:

$$k_G = 0.9926 + 0.03794 \left(\frac{2R}{z}\right)^2 \quad (26)$$

Where R is the rotor radius and z is the height above the ground.

Secondly, Nohabari & Sharafi's [22] model for small quadrotors, which adapted Hayden's model by a change in term k_G, accounting for a greater equivalent rotor radius in computing the coefficient to magnify the effect of the ground for the quadcopter:

$$k_G = 0.9926 + 0.03794 \left(\frac{5R}{z}\right)^2 \quad (27)$$

In Figure 15, the ratio of power required for hovering in ground effect (P_{IGE}) versus hover out of ground effect (P_{OGE}) is evaluated for increasing height above ground (normalised by rotor diameter, D). It is seen that the power tends towards the out-of-ground-effect requirement by 3.5 D height above ground. At 1.4 D height above ground, 8.7% less power is required to maintain the same amount of thrust.

It is seen that Nohabari & Sharafi's model matches the data trend quite well. In comparison, Hayden's helicopter model overpredicts the power requirement of the UAV as it underpredicts the height envelope of aerodynamic ground effect.

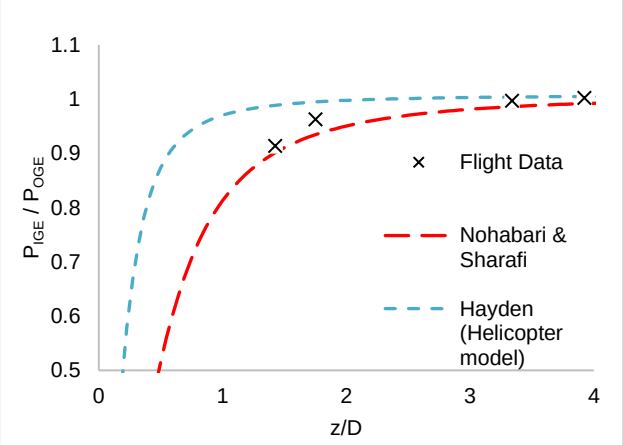

Figure 15: Power requirement in ground vicinity

6.2. Outdoor testing in windy conditions

Following successful indoor flight testing, the UAV was tested outdoors at Hans Christian Anderson Airport in Odense, Denmark in May 2024, as shown in Figure 16.

Figure 16: Outdoor flight test of FC-100 UAV in Odense, Denmark (May 2024). Video available from [26]: https://youtu.be/qPeQeakvhyE?si=TeDoAOQP-pLPtuzLm

6.2.1. Hover performance

Several flights were conducted with the FC-100 outdoors in windy conditions. The wind speed and direction were measured at the beginning of each test using an anemometer and wind vane. To assess the power performance, the Rotax 915 operators manual offers an empirical formula for calculating the instantaneous engine power, P_e, during flight using the measured air flow rate at the engine intake [27]:

$$P_e\ [kW] = -6.3264 + 0.0169\ Q\ [gal/min] \quad (28)$$

Where Q is the measured air flow rate.

An estimate of the instantaneous total thrust produced by the four rotors is found by calculating the estimated thrust of each rotor at its instantaneous rotational speed (using Eq. 9) and then summing these values. Note that this estimate assumes no effect of the wind.

Table 4: Outdoor hover flight data

W $[kg]$	**T** $[kg]$	$\boldsymbol{P_e}$ $[kW]$	$\boldsymbol{LE_e}$ $\left[\frac{kg}{kW}\right]$	$\boldsymbol{LE_e}$ calc[a] $\left[\frac{kg}{kW}\right]$	$\boldsymbol{\Delta LE_e}$ [%]
Flight (1): $V_{wind} = 11.2$ m/s, 158° heading					
423	459	78.5	5.8	6.9	21
Flight (2): $V_{wind} = 2.9$ m/s, 135° heading					
439	488	82.9	5.9	6.6	11

[a]*Prediction of rotor effective lift efficiency calculated using power curve fit (see Figure 8).*

The results from two hovering flights at different wind speeds are presented, detailed in Table 4. In both flights, the altitude was over 10 m which is assumed to be outside of the ground effect region, taken to be 8.2 m based on 3.5D height above ground (see Section 6.1).

The vehicle take-off weight was different between flights, due to differences in liquid fuel weight. The calculated total thrust produced by the rotors is greater than the vehicle take-off weight in both cases. This may be due to the increased thrust required to maintain the vehicle at a non-zero attitude during the hover, to produce a horizontal component of thrust to counteract the wind forces on the UAV. However, the estimate of thrust does not account for changes in efficiency and measurement variation due to the wind conditions, which may also explain this effect.

The difference in effective lift efficiency between the two flights is negligible (<2%), within the error margins of the instrumentation. This suggests little impact on lift efficiency of wind speeds up to 11.2 m/s.

Comparison is made between the effective lift efficiency data and predicted values for both flights, calculated using the curve fit for the isolated rotor data (see Figure 8). A large difference of 21% and 11% for flights (1) and (2) is found, respectively. There are several factors which likely contribute to this difference: the engine power measurement which is used to calculate the effective lift efficiency includes the auxiliary power required for on-board avionics and cooling fans (< 2kW). The predicted value only accounts for the power requirement of the rotors; the estimated thrust used to calculate the effective lift does not account for changes in efficiency and measurement variation due to the wind conditions, which may be significant; the rotors may be less efficient on the UAV due to rotor wake interactions and rotor-fuselage interactions. Research on small propellers noted a decrease in thrust of 2% when the tip-to-tip spacing between rotors on the airframe is less than 10% of rotor diameter [28]. The FC-100 has a minimum tip-to-tip spacing of 4.3% of rotor diameter, so this effect may merit further investigation.

Overall, it has been demonstrated that the UAV can sustain hover in wind at least up to 11.2 m/s without substantial decrease in the effective lift efficiency. This result demonstrates potential for the UAV to operate effectively in windy environments.

6.2.2. Translational flight performance

A short translational flight was conducted in the same wind conditions as flight (1) in Figure 17. The UAV attitude commands are manually sent via an RC link, with active attitude stabilisation by the flight controller. The UAV was commanded to take off and hover, followed by a short return trip flight at a 145° heading. The GPS data from the flight is graphically plotted on Google Earth, with vertical bars denoting altitude (see Figure 17).

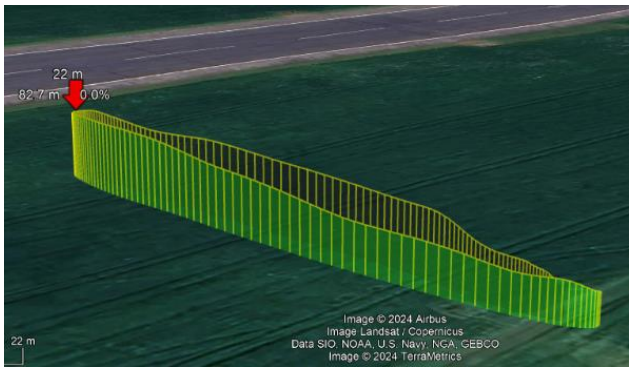

Figure 17: GPS data showing outdoor flight path. Vertical lines denote altitude.

As shown in Figure 18, during the outbound portion of the flight, the UAV accelerates from stationary to a maximum ground speed of 7.44 m/s (26.8 km/h) before decelerating, and on the inbound return flight the UAV reached a maximum ground speed of 8.14 m/s (29.3 km/h). The altitude increases during the initial acceleration, remains fairly constant, then reduces during the deceleration phase of the return flight.

The airspeed, shown in Figure 18, is calculated by summation of the ground velocity vector with the component of the wind vector projected in the direction of the flight:

$$\vec{v}_{air} = \vec{v}_{ground} + \vec{v}_{wind}\cos(\alpha° - \beta°) \qquad (29)$$

Where $\alpha°$ is the bearing heading of the wind and $\beta°$ is the bearing heading of the flight.

During the outbound portion of the flight, the airspeed is negative, meaning that there is a net positive drag force acting on the UAV in the direction of flight. In comparison, on the inbound portion of the flight, the airspeed reaches a maximum of 18.2 m/s (65.5 km/h), with a negative drag force on the UAV. The discontinuity in airspeed shown is due to the change in vehicle direction.

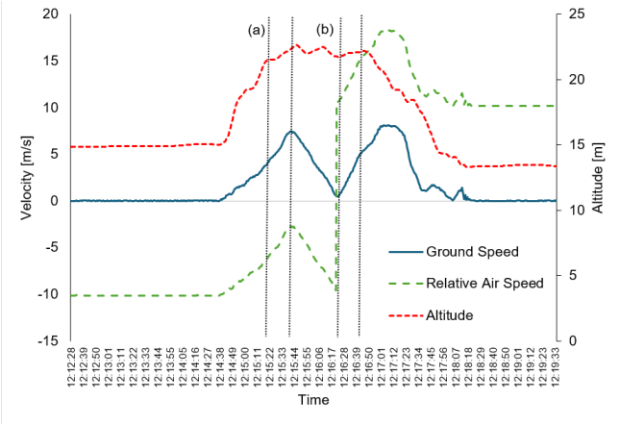

Figure 18: Ground speed, airspeed and altitude vs time

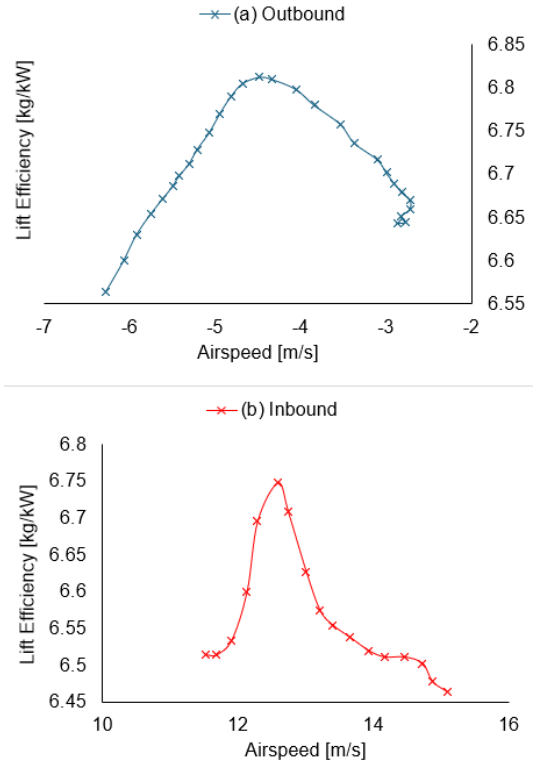

Figure 19: Lift efficiency versus airspeed during flight (a) outbound (top) & (b) inbound (bottom)

As the flights were conducted manually with a remote UAV pilot, the altitude was not maintained precisely which limits the ability to compare between flights. The lift efficiency is compared for two portions of the flight, marked by the segments (a) and (b) in Figure 18. Segment (a) occurs during the outbound flight, with negative airspeed, and segment (b) occurs during the inbound flight with positive airspeed. The instantaneous lift efficiency during both flight segments is compared against the airspeed, shown in Figure 19.

It is noted that the lift efficiency increases overall during the outbound portion of the flight, by 4.4% to a maximum before reducing to a value 1.9% higher than initially. The increasing lift efficiency benefit may be attributed to the positive drag force on the UAV due to the tailwind, which acts to propel the UAV forward through the air, thus requiring a lower power input to the rotors to achieve the same acceleration. It is not clear why there is a rise and fall in lift efficiency during this flight phase, but it may be explained partially by any benefits in lift efficiency gained during forward flight reducing as the absolute value of the airspeed decreases, or due to the additional power requirements for a climb in altitude during this flight segment.

During the inbound portion of the flight (b), the UAV flew with a headwind. The lift efficiency increases initially by 3.4% as the UAV accelerates, which may be attributed to the increase in lift efficiency of the rotor as the airspeed increases. After reaching a peak in lift efficiency, it begins to decrease as the UAV continues to accelerate, eventually reaching a value at the end of the segment with negligible difference than at the beginning. Similarly to the outbound portion of flight (a), it is not clear why this occurs, but it may be due to improvements in lift efficiency of the rotor being balanced by the increasing parasitic drag of the UAV as the airspeed increases.

It is worth noting that during both flight segments studied, the UAV is accelerating and not in steady-state flight. Future work will focus on analysing the aerodynamic efficiency of the rotors during the transition into forward flight and performance at a steady state cruise speed. Some further limitations of the outdoor flight testing are that: no flights were completed with low or zero wind speed, so comparison against a ‘static’ control data set is not possible at this stage; the flights were conducted manually by a remote UAV pilot. Improvement in automated flight control systems will improve repeatability of data collection; no data was collected at a steady state forward flight speed with constant altitude. Due to this, comparisons cannot be made at this time with the trailer test data for the single rotor (Section 5).

Overall, study of the lift efficiency during two portions of flight in windy conditions has shown no measurable decrease in performance across the flight conditions tested, even during vehicle acceleration. This data demonstrates a reliable performance of the FC-100

UAV for its intended application in windy offshore environments as a utility cargo drone.

7. CONCLUSIONS

1. A working demonstrator of the FC-100 UAV is presented with a multirotor design and Digital Displacement® hydraulic transmission to convert power from an engine to lifting rotors. An experimental campaign was conducted to investigate the aerodynamic performance of a single isolated rotor and the full-scale FC-100 system.

2. The Figure of Merit (FM) of the isolated rotor is found to be above 73% within its operational speed range. The data shows a decrease in the FM with higher speed, which is attributed to changes in the effective blade geometry at higher loading.

3. The experimental campaign demonstrates that the lift efficiency of the isolated rotor improves with increasing forward flight velocity, with the greatest improvement for the edgewise flight case and the effect decreasing as the rotor disc is tilted forward into the free-stream flow. To the best of the authors' knowledge, this study is the first to experimentally verify this improvement in lift efficiency in forward flight for fixed-pitch rotors with a diameter greater than 2 metres.

4. This experimental campaign is the first to evaluate the aerodynamic ground effect for a large quadrotor UAV. The power requirement to maintain constant altitude hover of the FC-100 is reduced when hovering at a distance above ground up to 3.5 rotor diameters. It further demonstrates that published models describing ground effect for small quadrotor UAVs may be valid for performance prediction in large scale quadrotor UAVs too.

5. The FC-100 has shown reliable performance in terms of lift efficiency in both continuous hovering and in forward flight within a range of wind velocities. This demonstrates the platform's suitability for intended logistics applications in harsh offshore environments.

8. OUTLOOK

Outdoor flight testing of the FC-100 platform began in the UK in August 2024 under CAA operational authorisation. These tests will focus on the use of automated flight control systems which will enable improvements in data quality and repeatability for analysis of flight performance. Operation at higher flight speeds and wider environmental conditions will be evaluated.

The next design iteration of the FC-100 platform is finishing assembly at Flowcopter's manufacturing facility in Edinburgh, Scotland. This platform features an improved rotor design and lightweighting of mechanical components, enabling a predicted 250 kg maximum payload cargo capacity. Testing of the UAV will begin late 2024.

Author contact:

Calum Arnott* - calum.arnott@flowcopter.com

Rory Haggart - rory.haggart@flowcopter.com

Robert Courtney - robert.courtney@flowcopter.com

Uwe Stein - uwe.stein@flowcopter.com

Francisca Martinez-Hergueta – francisca.mhergueta@ed.ac.uk

9. ACKNOWLEDGMENTS

This work has been supported by an Innovate UK SMART grant, project no. 10054955.

10. REFERENCES

[1] M. Hirschberg, 'Press Release: Vertical Flight Society Electric VTOL Directory Hits 1,000 Designs', Electric VTOL News by the Vertical Flight Society. Accessed: Jul. 20, 2024. [Online]. Available: https://evtol.news/news/press-release-vertical-flight-society-electric-vtol-directory-hits-1000-designs

[2] M. Burston, K. Ranasinghe, A. Gardi, V. Parezanović, R. Ajaj, and R. Sabatini, 'Design principles and digital control of advanced distributed propulsion systems', *Energy*, vol. 241, p. 122788, Feb. 2022, doi: 10.1016/j.energy.2021.122788.

[3] H. D. Kim, A. T. Perry, and P. J. Ansell, 'A Review of Distributed Electric Propulsion Concepts for Air Vehicle Technology', in *2018 AIAA/IEEE Electric Aircraft Technologies Symposium (EATS)*, Jul. 2018, pp. 1–21. Accessed: Jul. 20,

* Corresponding author

2024. [Online]. Available: https://ieeexplore.ieee.org/abstract/document/8552794
[4] N. Caldwell, P. McCurry, U. Stein, and D. Rancourt, ‘Digital Displacement Hydrostatic Transmission for Rotorcraft and Distributed Propulsion’, in *Vertical Flight Society Annual Forum & Technology Display - Forum 77*, The Vertical Flight Society, 2021. doi: 10.4050/F-0077-2021-16890.
[5] N. Caldwell, P. McCurry, U. Stein, and D. Menzies, ‘Ground-based tests of a digital displacement hydraulic transmission for distributed propulsion’, in *47th European Rotorcraft Forum 2021*, European Rotorcraft Forum, Jul. 2021.
[6] W. H. S. Rampen, ‘Digital displacement hydraulic piston pump’, 1992, Accessed: Mar. 05, 2024. [Online]. Available: https://era.ed.ac.uk/handle/1842/12829
[7] N. J. Caldwell, ‘Digital displacement hydrostatic transmission systems’, PhD Thesis, University of Edinburgh, 2007. Accessed: Jul. 20, 2024. [Online]. Available: https://era.ed.ac.uk/handle/1842/27735
[8] N. Caldwell, ‘Review of Early Work on Digital Displacement® Hydrostatic Transmission Systems’, in *BATH/ASME 2018 Symposium on Fluid Power and Motion Control*, Bath: American Society of Mechanical Engineers Digital Collection, Nov. 2018. doi: 10.1115/FPMC2018-8922.
[9] J. G. Leishman, *Principles of Helicopter Aerodynamics*. Cambridge University Press, 2002.
[10] J. Seddon and S. Newman, *Basic Helicopter Aerodynamics, 3rd Edition*. John Wiley & Sons, 2011.
[11] D. Han and G. N. Barakos, ‘Comparison of design features of quadrotor aircraft and helicopters from the point of view of flight performance’, in *47th European Rotorcraft Forum 2021*, European Rotorcraft Forum, 2021.
[12] D. Han, L. Zhou, and G. N. Barakos, ‘Parametric Investigation of the Flight Performance of a Variable Rotor Pitch X-Configuration Quadrotor Aircraft’, *J. Aerosp. Eng.*, vol. 35, no. 6, p. 04022082, Nov. 2022, doi: 10.1061/(ASCE)AS.1943-5525.0001481.
[13] P. Pounds, R. Mahony, and P. Corke, ‘Modelling and control of a large quadrotor robot’, *Control Eng. Pract.*, vol. 18, no. 7, pp. 691–699, Jul. 2010, doi: 10.1016/j.conengprac.2010.02.008.
[14] J. Y. Hwang, M. K. Jung, and O. J. Kwon, ‘Numerical Study of Aerodynamic Performance of a Multirotor Unmanned-Aerial-Vehicle Configuration’, *J. Aircr.*, vol. 52, no. 3, pp. 839–846, 2015, doi: 10.2514/1.C032828.
[15] D. H. Nguyen, Y. Liu, and K. Mori, ‘Experimental Study for Aerodynamic Performance of Quadrotor Helicopter’, *Trans. Jpn. Soc. Aeronaut. Space Sci.*, vol. 61, no. 1, pp. 29–39, 2018, doi: 10.2322/tjsass.61.29.
[16] D. Shukla and N. Komerath, ‘Multirotor Drone Aerodynamic Interaction Investigation’, *Drones*, vol. 2, no. 4, Art. no. 4, Dec. 2018, doi: 10.3390/drones2040043.
[17] M. Misiorowski, F. Gandhi, and A. A. Oberai, ‘Computational Study on Rotor Interactional Effects for a Quadcopter in Edgewise Flight’, *AIAA J.*, vol. 57, no. 12, pp. 5309–5319, Dec. 2019, doi: 10.2514/1.J058369.
[18] Flowcopter, *Flowcopter FC100 Untethered Flight - YouTube*. Accessed: Jul. 20, 2024. [Online Video]. Available: https://www.youtube.com/watch?si=eRTTbKu0SB7nePJF&v=SsixCnzBZb0&feature=youtu.be
[19] I. C. Cheeseman and W. E. Bennett, ‘The effect of the ground on a helicopter rotor in forward flight’, 1955, Accessed: Jul. 31, 2024. [Online]. Available: https://reports.aerade.cranfield.ac.uk/handle/1826.2/3590
[20] J. S. Hayden, ‘The Effect Of The Ground On Helicopter Hovering Power Required’, in *Proceeding of AHS 32nd annual forum*, Washington, DC, USA, May 1976. Accessed: Jul. 20, 2024. [Online]. Available: https://www.semanticscholar.org/paper/The-Effect-Of-The-Ground-On-Helicopter-Hovering-Hayden/f59001cfbc848e8c0b200d2493910cc3d2e38fe1
[21] B. M. Kutz, F. Bensing, M. Keßler, and E. Krämer, ‘CFD Calculation of a Helicopter Rotor Hovering in Ground Effect’, in *New Results in Numerical and Experimental Fluid Mechanics VIII: Contributions to the 17th STAB/DGLR Symposium Berlin, Germany 2010*, A. Dillmann, G. Heller, H.-P. Kreplin, W. Nitsche, and I. Peltzer, Eds., Berlin, Heidelberg: Springer, 2013, pp. 297–304. doi: 10.1007/978-3-642-35680-3_36.
[22] H. Nobahari and A. R. Sharifi, ‘Continuous ant colony filter applied to online estimation and compensation of ground effect in automatic landing of quadrotor’, *Eng. Appl. Artif. Intell.*, vol. 32, pp. 100–111, Jun. 2014, doi: 10.1016/j.engappai.2014.03.004.
[23] P. Sanchez-Cuevas, G. Heredia, and A. Ollero, ‘Characterization of the Aerodynamic Ground Effect and Its Influence in Multirotor Control’, *Int. J. Aerosp. Eng.*, vol. 2017, no. 1, p. 1823056, 2017, doi: 10.1155/2017/1823056.
[24] X. He, G. Kou, M. Calaf, and K. K. Leang, ‘In-Ground-Effect Modeling and Nonlinear-Disturbance Observer for Multirotor Unmanned Aerial Vehicle Control’, *J. Dyn. Syst. Meas. Control*, vol. 141, no. 071013, May 2019, doi: 10.1115/1.4043221.
[25] Y. Tanabe, H. Sugawara, S. Sunada, K. Yonezawa, and H. Tokutake, ‘Quadrotor Drone Hovering in Ground Effect’, *J. Robot.*

Mechatron., vol. 33, no. 2, pp. 339–347, Apr. 2021, doi: 10.20965/jrm.2021.p0339.
[26] Flowcopter, *Flight Trials of the Flowcopter FC100 Heavylift Cargo Drone at UAS Denmark Test Center - YouTube*. Accessed: Jul. 20, 2024. [Online Video]. Available: https://www.youtube.com/watch?v=qPeQeak-vhyE&ab_channel=Flowcopter
[27] Rotax, 'Operators Manual (OM) for ROTAX Engine Type 915 i A / C24 Series'. Dec. 07, 2022. [Online]. Available: https://www.fly-rotax.com/p/service/technical-documentation
[28] W. Zhou, Z. Ning, H. Li, and H. Hu, 'An Experimental Investigation on Rotor-to-Rotor Interactions of Small UAV Propellers', in *35th AIAA Applied Aerodynamics Conference*, in AIAA AVIATION Forum. , American Institute of Aeronautics and Astronautics, 2017. doi: 10.2514/6.2017-3744.

APPENDIX A – MOTOR EFFICIENCY DATA

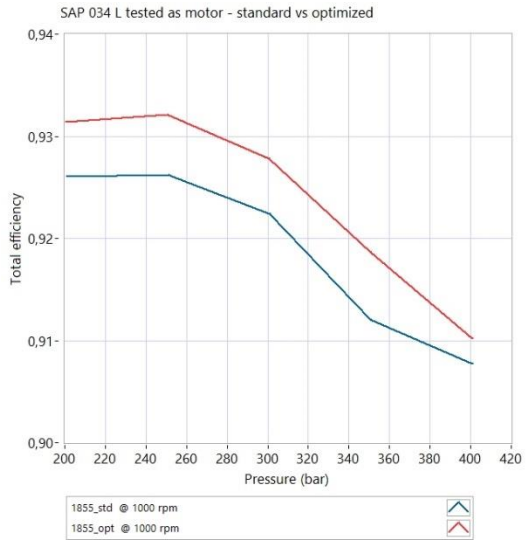

Figure 20 - Sunfab SAP034 efficiency curve at 1000 rpm